


Research Paper

Versatile pH-response Micelles with High Cell-Penetrating Helical Diblock Copolymers for Photoacoustic Imaging Guided Synergistic Chemo-Photothermal Therapy

Shengyu Shi^{1*}, Yajing Liu^{2*}, Yu Chen¹, Zhihuang Zhang¹, Yunsheng Ding¹, Zongquan Wu¹, Jun Yin¹, and Liming Nie²

1. Department of Polymer Science and Engineering, School of Chemistry and Chemical Engineering, Hefei University of Technology and Anhui Key Laboratory of Advanced Functional Materials and Devices, Hefei, 230009, China.
2. State Key Laboratory of Molecular Vaccinology and Molecular Diagnostics & Center for Molecular Imaging and Translational Medicine, School of Public Health, Xiamen University, Xiamen, 361102, China.

*These authors contributed equally to this work.

 Corresponding authors: Jun Yin: yinjun@hfut.edu.cn; Liming Nie: nielm@xmu.edu.cn© Ivyspring International Publisher. Reproduction is permitted for personal, noncommercial use, provided that the article is in whole, unmodified, and properly cited. See <http://ivyspring.com/terms> for terms and conditions.

Received: 2016.06.28; Accepted: 2016.07.30; Published: 2016.09.13

Abstract

With high optical absorption efficiency, near infrared (NIR) dyes have been proposed as theranostic agents for fluorescence imaging, photoacoustic imaging (PAI), and photothermal therapy (PTT). However, inherent hydrophobicity and short circulation time of small molecule hinder the further biomedical application. Herein smart amphiphilic copolymer was synthesized containing IR780/camptothecin@poly(ϵ -caprolactone) (IR780/CPT@PCL) as core, helical poly(phenyl isocyanide) (PPI) blocks as shell with the pH-responsive rhodamine B (RhB) moieties in the core-shell interface. With hydrophilic helical PPI coronas, these micelles present significantly enhanced cell-penetrating capacity that plays a key role in facilitating intracellular delivery of various cargos. By encapsulating CPT and IR780 molecules, the multifunctional self-assemble probe has huge potential to realize functional cooperativity and adaptability for cancer diagnosis and therapy. The *in vitro* and *in vivo* experimental results demonstrate that the pH-triggered fluorescent responsiveness and strong acoustic generation permit them efficient fluorescent and PA signal sensing for cancer diagnosis. Moreover, with 808 nm laser irradiation, the generated heat significantly improves the drug release from PCL core, leading to synergetic chemo-photothermal therapy and decreases tumor recurrence rates in mice. Overall, the biocompatible multifunctional micelles with these combined advantages can potentially be utilized for PAI guided disease diagnosis and tumor ablation.

Key words: helical poly(phenyl isocyanide), micelles, cell penetration, photoacoustic imaging, theranostics.

Introduction

Photoacoustic (PA) imaging (PAI) is a new biomedical imaging modality that noninvasively measures the ultrasonic waves induced by tissue absorption of laser light and maps the optical absorption distribution.^[1-3] Ideally, PAI probes should have high potential to convert the absorbed laser into heat and produce ultrasound signals. NIR-absorbing molecules, such as indocyanine green (ICG),

methylene blue (MB), and Evans blue (EB), lying in the wavelength range of 650 to 900 nm, can provide better sensitivity for *in vivo* imaging and monitoring, have been widely utilized in PAI.^[4-6] However, development of versatile exogenous PA contrast agents with excellent biocompatibility and versatility still remains an open quest for specific application purposes.

With a rigid cyclohexenyl ring in the heptamethine chain, IR-780 has higher fluorescence intensity and more stable structure than ICG.^[7-9] As a NIR sensor, IR-780 has also been applied on PAI because of the high optical absorption and its proper NIR absorption peak. Moreover, upon NIR laser irradiation, the energy of the laser can be efficiently converted to heat, allowing it to be utilized in photothermal therapy (PTT).^[10] On the downside, the lipophilicity and short retention time limit its biomedical application.^[11-13] In addition, the notable nonspecificity raises concerns regarding unnecessary harm to healthy tissue, which is another pressing obstacle for cancer diagnosis and therapy.^[14]

Compared with a single chromophore or light-absorbing compound, a self-organized structure can encapsulate several types of functional molecules into a single assembly and is further the purpose of targeted therapy.^[8, 15, 16] Owing to their excellent biocompatibility and structural versatility, self-assembled micelles have been implemented in biomedical diagnosis and therapy to realize functional cooperativity and adaptability.^[17, 18] The hydrophilic polyethylene glycol (PEG), a FDA approved compound, has been introduced as attractive method for helping IR-780 self-assemble into micelles, which increases water solubility and protects it from fast metabolism *in vivo*.^[12, 19] To most micelles delivery systems, the cell-penetrating capacity is crucial to cell uptake and thus has a giant impact on tumor accumulation. However, the cell-penetrating ability of existing micelles still cannot meet the demand in many biological applications. Moreover, the size of micelles is a tradeoff between the enhanced permeability and retention (EPR) effect and drug loading.

Cell-penetrating peptides (CPPs) are oligopeptides consisting of 10-30 amino acid residues that have excellent cell membrane permeability. They can either adopt helical structures or form helices in the cell membranes to promote permeability in various mammalian cells.^[20-23] The helix is the ubiquitous structural motif for biological polymers, however to the best of our knowledge the cell membrane permeability of micelles with helical chains has not been studied nor applied *in vivo*.^[24, 25]

As an effective artificial helical polymer, PPI plays key roles in their sophisticated functions, such as chiral recognition, asymmetric catalysis, and biomedical applications.^[26-29] We envision that PPI is very attractive for IR-780 micelles due to two main reasons: (1) with a distinctive π -conjugated system, PPI has an inherently stable helical conformation in aqueous solution or in solid state, which has a structural similarity to CPPs.^[30, 31] Therefore,

introducing hydrophilic helical PPI chains in the micelle shell would facilitate intracellular delivery of cargos and create an artificial synthetic helical polymer-based delivery system. (2) Compared with hydrophilic PEG chains, PPI chains have side chains easy to modify, which can be substituted by different functional groups to achieve versatile biological functions, such as targeting or molecular recognition.^[32]

In this work, we developed a versatile agent based on IR780@PPI(-rhodamine)-b-poly(ϵ -caprolactone) IR780@PPI(-RHB)-PCL (IM) micelles, with helical PEGylated phenyl isocyanide (PI) as hydrophilic shell and CPT/IR780@PCL as hydrophobic core. To the best of our knowledge, PPI is for the first time to be applied for developing novel biocompatible hybrid block copolymers and even for bio-medical applications. Amphiphilic diblock copolymer PPI(-RHB)-PCL (PM) containing structurally stable hydrophilic helical PPI block was synthesized. It was two mechanistically distinctive "one-pot" living polymerization process through copolymerization of PEGylated PI and ϵ -CL monomers by a novel bifunctional catalyst, CIPd(PET₃)₂-RhB-OH. This catalyst contained a Pd(II) active center, a hydroxyl group, and a pH-responsive RhB moiety anchored in the core-shell interface. Surprisingly, the RhB moieties in the micelles with original ring-closed form (nonfluorescent) can be selectively converted into the fluorescent ring-opened form in acidic environment of tumor cells and served as a fluorescence "turn-on" probe. Using a co-solvent self-assembly approach, IR780 molecules were encapsulated and thus spherical IM were formed. In this novel copolymer, the hydrophilic helical PPI coronas enable these micelles superior cell membrane permeability. The strong stimuli-triggered fluorescent responsiveness and innate NIR absorption allow them to be served as an efficient fluorescent probe, PAI contrast agent and PTT carrier (Scheme 1).

In many case, PTT alone could not efficiently destroy all cancer cells and might lead residual cells to survive in the long term. PTT combined with chemotherapy has emerged as an optimized approach to generate a synergistic effect for cancer therapy.^[15] To realize chemo-photothermal synergetic therapy, IR780/CPT@PPI(-RHB)-PCL (ICM) micelles were further fabricated which can simultaneously deliver chemotherapeutic drug and photothermal agent to tumor site (Scheme 1). Upon NIR laser irradiation, the generated heat largely enhanced the drug release from PCL core and decreased tumor recurrence rates. Therefore, the newly developed multifunctional integrated platform with these combined advantages can be utilized as a promising approach to disease

diagnosis and ablation of tumor tissue.

Materials and methods

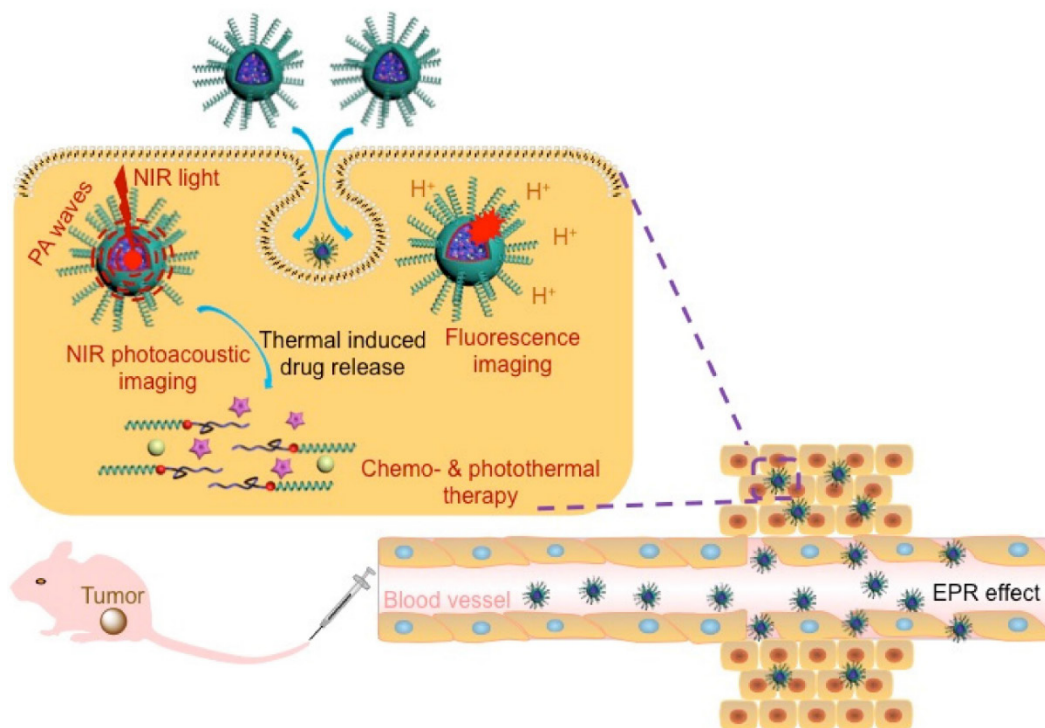
Materials

All solvents were obtained from Sinopharm. RhB hydrochloride, Nile red, IR780, camptothecin (CPT), ethylenediamine, 2-bromoethanol, 1-ethyl-3-(3-dimethylaminopropyl) carbodiimide hydrochloride (EDCI), N-hydroxybenzotriazole (HOBT), trifluoroacetic acid (TFA), potassium carbonate, dicyclohexylcarbodiimide (DCC), 4-dimethylaminopyridine (DMAP), stannous octanoate ($\text{Sn}(\text{Oct})_2$), ϵ -caprolactone (ϵ -CL), methoxypolyethylene glycol (mPEG-OH; $M_n = 1,900$ g/mol), and *trans*-dichlorobis(triethylphosphine) palladium(II) were purchased from Aladdin and Sigma-Aldrich. Female BALB/c athymic mice (5-6 weeks old) were purchased from Si Laike Laboratory Animal Co. Ltd. (Shanghai, China). All *in vivo* experimental procedures were conducted in accordance with the animal care and use guidance of Xiamen University.

Synthesis of palladium(II) modified complex $\text{CIPd}(\text{PET}_3)_2\text{-RhB-OH}$

The rhodamine-encoded bifunctional catalyst $\text{CIPd}(\text{PET}_3)_2\text{-RhB-OH}$ bearing a Pd(II) active center and a hydroxyl group was synthesized from rhodamine B hydrochloride by sequential chemical

modification (scheme S1a).^[31, 33-35] The chemical structure of the intermediates (1-8) during the catalyst preparation were verified by ^1H NMR spectra, and the exact structure of the final $\text{CIPd}(\text{PET}_3)_2\text{-RhB-OH}$ was confirmed by ^1H NMR, ^{13}C NMR, ^{31}P NMR, mass spectrometry (Figure S1), and FT-IR spectrometry (Figure S2). ^1H NMR (600 MHz, CDCl_3 , 25 °C; Figure S1a): δ 8.01-7.96 (d, 1H, ArH), 7.50-7.39 (m, 4H, ArH), 7.23-7.16 (m, 3H, ArH), 7.06-7.03 (d, 1H, ArH), 6.35-6.03 (m, 6H, ArH), 4.42 (s, 1H, ArCH), 3.70 (m, 2H, $-\text{CH}_2\text{CH}_2\text{OH}$), 3.44-3.24 (m, 12H, $-\text{N}(\text{CH}_2\text{CH}_3)_2$, $-\text{NCH}_2-$, $-\text{NHCH}_2\text{CCH}$), 2.91-2.63 (m, 4H, $-\text{NHCH}_2-$, $-\text{CH}_2\text{CH}_2\text{OH}$), 1.93-1.87 (m, 12H, $-(\text{PCH}_2\text{CH}_3)_2$), 1.19-1.11 (m, 18H, $-(\text{PCH}_2\text{CH}_3)_2$), 1.15 (q, 12H, $-\text{N}(\text{CH}_2\text{CH}_3)_2$). ^{13}C NMR (150 MHz, CDCl_3 , 25 °C; Figure S1b): δ 174.88, 173.07, 156.52, 155.95, 155.63, 151.53, 140.33, 135.58, 132.84, 131.55, 131.00, 130.93, 130.35, 126.55, 125.56, 110.56, 106.78, 100.27, 100.10, 75.43, 68.58, 61.82, 53.99, 47.00, 46.97, 44.13, 43.56, 41.56, 18.09, 18.00, 17.91, 15.24, 15.16, 11.00, 2.66. FT-IR (KBr, 25 °C; Figure S2): 3428, 2968, 2931, 2867, 2119, 1673, 1633, 1616, 1545, 1513, 1468, 1452, 1427, 1396, 1377, 1355, 1331, 1302, 1267, 1223, 1153, 1120, 1090, 1074, 1034 cm^{-1} . HRMS m/z (Figure S1d): calcd for $\text{C}_{55}\text{H}_{78}\text{ClN}_5\text{O}_4\text{P}_2\text{Pd}$ $[\text{M}+\text{H}]^+$, 1076.4252; found: 1076.4674. Anal. Calcd (%) for $\text{C}_{55}\text{H}_{78}\text{ClN}_5\text{O}_4\text{P}_2\text{Pd}$: C, 61.33; H, 7.30; N, 6.50; Found (%): C, 61.31; H, 7.28; N, 6.48.



Scheme 1. Schematic representation of ICM for multi-mode imaging guided synergistic chemo-photothermal treatment of tumors upon their internalization by cells via endocytosis.

One-pot copolymerization of PEGylated isocyanide monomers and ϵ -CL with $\text{CIPd}(\text{PEt}_3)_2\text{-RhB-OH}$ as catalyst

Typically, a 10 mL oven-dried flask was charged with catalyst 7 (9.2 mg, 0.009 mmol), ϵ -CL (41 mg, 0.36 mmol; $[\text{M}]_0/[\text{I}]_0 = 40$), monomer 9 (93.63 mg, 0.32 mmol; $[\text{M}]_0/[\text{I}]_0 = 35$), and anhydrous 1,2-dichloroethane (5.0 mL). To this stirring mixture was added a solution of $\text{Sn}(\text{Oct})_2$ (0.018 mmol) in 1,2-dichloroethane *via* a syringe at ambient temperature. After stirred at 80 °C for 24 hours, the polymerization solution was precipitated into a large amount of cold diethyl ether, collected by centrifugation, and dried in vacuum at ambient temperature overnight to afford the diblock copolymer PPI(-RhB)-PCL. For control samples, amphiphilic PPI-PCL copolymers were prepared by one-pot living polymerization of PEGylated phenyl isocyanide (PI; 9) and ϵ -CL monomers with $\text{CIPd}(\text{PEt}_3)_2\text{-OH}$. The mPEG-PCL copolymers were synthesized with mPEG as macroinitiator.

Self-assembly of PPI(-RhB)-PCL diblock copolymers

Typically, 2.0 mg of diblock copolymer was dissolved in 0.5 mL of DMF, the solution was stirred and maintained for 30 min at room temperature. Under vigorous stirring, 1.5 mL of DI water was added *via* a syringe pump at a flow rate of 0.05 mL/min. After the addition was completed, the dispersion was left stirring for another 12 h. DMF was then removed by dialysis (MWCO 3.5 kDa) against pure water for 24 h.

Preparation of Near Infrared Dyes (IR780) and Anti-Cancer Drug (CPT) Loaded Polymeric Micelles

Hydrophobic IR780 and CPT molecules were loaded into the hydrophobic PCL cores during the self-assembly process. Typically, the THF solutions of PPI(-RhB)-PCL diblock copolymers (20 g/L), IR780 (2.0 g/L), and CPT (4.0 g/L) were prepared in advance, respectively, and mixed together. A similar self-assembly procedure was performed upon a slow DI water addition as mentioned above. The final mixture was vacuumed to remove the organic solvent. Free IR780 and CPT were removed by passing through a 0.22 μm Millipore filter. The final micellar dispersion was diluted with phosphate buffer solution (PBS; pH 7.4).

In vitro drug release profile of CPT from the ICM with and without laser irradiation

The CPT release from ICM was measured by the dialysis method. Briefly, ICM micellar dispersion (0.5

g/L in PBS; 5 mL) was placed in a dialysis tube (MWCO is 3500 Da) and then immersed into 250 mL of PBS with Tween 20 (1% total volume) under gentle stirring at 37 °C. The system treated with or without laser irradiation (808 nm, 1 W cm^{-2}) was according to the need. At 0, 0.5, 1, 2, 3, 4, 5, 6, 7, 8, 9, 10, 11, and 12 h, 20 mL external buffer solution was removed and replaced with equal volume of fresh medium. The separated solution was lyophilized and then dissolved in DMSO, the CPT concentration was quantified by measuring the absorbance at 355 nm against a standard calibration curve.

Preparation of Nile red-loaded polymeric micelles

Hydrophobic Nile red was loaded into the PPI-PCL or mPEG-PCL diblock copolymers during the co-solvent self-assembly process. Typically, take PPI-PCL for example, the initial concentrations of PPI-PCL and Nile red in THF were 2.0 and 0.01 g/L, respectively. A similar self-assembly procedure was then performed upon a slow DI water addition as detailed above. After removal of THF *via* dialysis (MWCO 3.5 kDa) against pure water, the Nile red@PPI-PCL micelle dispersion was stored for further use. Following the same procedure, Nile red@mPEG-PCL micelle dispersion was also prepared. The loading content for Nile red were calculated based on the emission spectra of Nile red (excitation: 550 nm) against a standard calibration curve.

Cell culture and *in vitro* cytotoxicity assessment of ICM

HeLa cells (5×10^3 cells/well) in Dulbecco's modified Eagle's medium (DMEM) complete medium were plated into a 96-well plate and incubated overnight. HeLa cells were then exposed to micelles (0, 0.2, 0.5, and 1.0 g/L) at 37 °C for up to 6 h in DMEM complete medium. Then, cells were rinsed with PBS buffer and DMEM complete medium. Cytotoxicity was assessed by adding 3-(4,5-dimethyl-2-thiazolyl)-2,5-diphenyl tetrazolium bromide (MTT) for another 4h. Cells incubated with PBS only were served as positive control. For comparison, the cytotoxicity of CPT, IM and PM were also assessed following the same procedures.

Pharmacokinetic studies

Seven or eight week-old ICR female mice were used to study the pharmacokinetic of ICM. At post-injection time (0.1 h, 1 h, 2 h, 4 h, 8 h, 10 h, 12 h and 24 h), blood samples were collected from the retro-orbital plexus of mouse eyes and were centrifuged (10 min, 3000 g). For analysis, the plasma

(100 μL) was exposed to 200 μL of acetonitrile. After vortexing for 10 s, 800 μL of chloroform was added. Upon centrifugation at 10,000 g for 5 min, the organic layer was carefully collected into 1.5 mL Eppendorf tubes and evaporated using centrifugal vacuum concentrators (Labconco CentriVap) at 30 $^{\circ}\text{C}$ for 2 h. The residue was dissolved in 200 μL of solution [acetonitrile: tetrahydrofuran $\frac{1}{4}$ $\frac{7}{3}$ (v/v)]. After centrifugation (10,000 g, 5 min), the supernatant was collected for HPLC (Waters ACQUITY) analysis. Standard curves were generated by the addition of free CPT at different concentrations, followed by extraction and quantification as mentioned above.

In vitro fluorescence imaging

Fluorescence images of PM internalized HeLa cells were acquired using an inverted Leica SP2 confocal microscope at 37 $^{\circ}\text{C}$. The samples were excited at 543 nm for RhB, and the fluorescence was collected between 555-600 nm for the red channel. All confocal laser scanning microscopy (CLSM) images were taken under the same conditions for parallel comparison. For Nile red@PPI-PCL and Nile red@mPEG-PCL samples, the fluorescence was excited at 550 nm.

Photothermal effect of ICM complex

The tumor temperature increase were determined 24 h after injecting ICM into tumor-bearing-mice. The mice administrated with 100 μL of PM or IM (equivalent to 10 mg/kg) *via* intravenous injection were designated as control. All of the tumor regions were exposed to 1 W/cm² NIR laser (λ = 808 nm) for 10 min. The changes of intratumoral temperature during laser irradiation were recorded with an infrared thermal image instrument. For cellular level test, after laser irradiation, cell injury was directly observed by calcein-AM and propidium iodide (PI) staining for 20 min. The live cells were stained with calcein-AM and dead cells were stained with PI.

Photoacoustic imaging

Different concentrations of ICM were detectable at 800 nm by the PAI. For *in vivo* PA test, PA images for tumors were captured at different time points using a hemispherical PAI system. Owing to the built-in hemispherical configuration, the PA system can acquire signals from various angles. To detect the accumulation of micelles in tumor, the mouse was anesthetized and placed in a plastic animal tray, which was placed inside the imaging bowl filled with deionized water to allow acoustic coupling.

In vivo biodistribution evaluation

When the tumor size was about 100-150 mm³, mice were administrated by intravenous injection of ICM, IM, or PM, respectively. The biodistribution of micelles in the HeLa tumor-bearing-mice was examined by fluorescent imaging and PA imaging at 4, 8, 12, 24, and 36 h after injection. The treated mice were sacrificed by cervical vertebra dislocation at 24 h after intravenous administration. The heart, liver, spleen, lung, kidneys, and tumor were harvested. The fluorescence intensity of different organs was analyzed by an IVIS Lumina II imaging system (Caliper Life Sciences, USA). Photothermal therapy (PTT) was performed when the tumor volume reached about 100-150mm³. The treated animals were divided into different groups to monitor antitumor efficacy. All micelles were intravenous administered to the mice, and the tumor sites were irradiated by 808 nm laser for 10 min after 24 h injection. The initialization of NIR laser was set as day 0. The body weight change and tumor volume were recorded continuously. After the treatments, the major organs and tumor of mouse were harvested, fixed in 4% formalin, and stained with hematoxylin and eosin (H&E).

Results and discussions

Preparation and characterization of micelles

The well-defined hydrophilic helical PPI containing amphiphilic diblock copolymers, PM, were prepared with controlled molecular weights (MWs) and tunable compositions. It was through orthogonal copolymerization of PI ($[\text{M}]_0/[\text{Cat.}]_0 = 35$) and ϵ -caprolactone ($\epsilon\text{-CL}$; $[\text{M}]_0/[\text{Cat.}]_0 = 40$) monomers simultaneously in one pot (Scheme S1). The RhB-encoded bifunctional catalyst CIPd(PET₃)₂-RhB-OH was synthesized by sequential chemical modification (Scheme S1a).^[36] The exact structure of CIPd(PET₃)₂-RhB-OH was confirmed by ¹H NMR, ¹³C NMR, ³¹P NMR, mass spectrometry (Figure S1), and FT-IR spectrometry (Figure S2). The chemical structure of the isolated copolymers was first analyzed by size-exclusion chromatograms (SEC; Figure 1A). The SEC trace of PM copolymers exhibited a monomodal elution peak with a number-average molecular weight (M_n) of 15.6 kDa and narrow MW distributions ($M_w/M_n = 1.19$). As compared to PM copolymers, the SEC traces of the PPI(-RhB)-OH and PCL(-RhB)-CIPd(PET₃)₂ homopolymers were located in the low MW region (Figure 1A). As expected, the sum of the MWs of the two homopolymers was in accordance with that of the PM copolymers (Table 1).

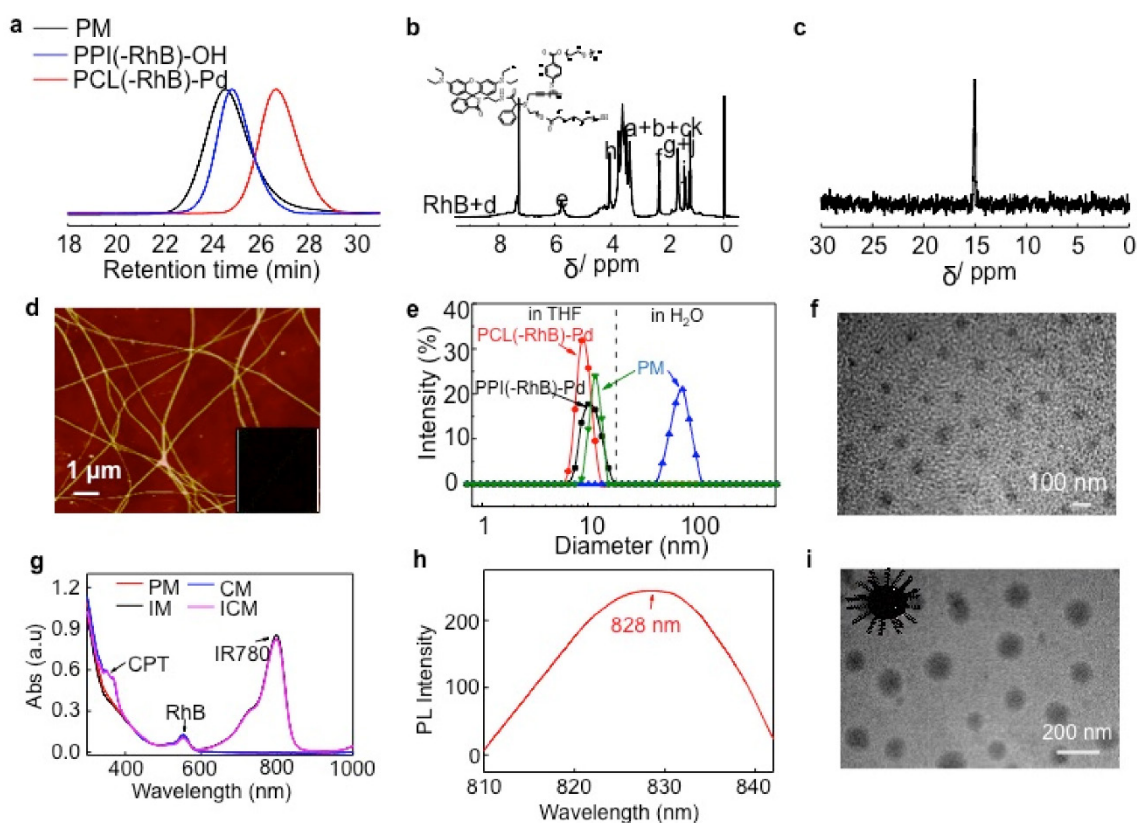


Figure 1. (A) SEC traces obtained for PM, PPI(-RhB)-OH, and PCL(-RhB)-CIPd(PET₃)₂ polymers, using THF as eluent. (B) ¹H and (C) ³¹P NMR spectra obtained for the PM diblock copolymers. (D) AFM image obtained for PM copolymers dried from THF solution, inserted image showed the magnified photo for the helical fibers. (E) DLS spectra obtained for PM, PPI(-RhB)-OH, and PCL(-RhB)-CIPd(PET₃)₂ polymers in THF or in water. (F) TEM image observed for PM dried from aqueous dispersion. (G) Absorption spectra recorded for PM, IM, CM, and ICM in water. (H) Fluorescent emission spectrum record for an aqueous dispersion of ICM (excitation = 790 nm). (I) TEM image observed for ICM dried from the aqueous dispersion.

Table 1. Molecular Parameters Summarized for Polymers.

run	[M ₁] ₀ /[Cat] ₀ ^a	[M ₂] ₀ /[Cat] ₀ ^a	M _n ^b (kDa)	M _w /M _n ^b	Yield ^c	Polymer
1	35	/	12.9	1.21	82 %	PPI ₃₂ (-RhB)-OH
2	/	40	4.60	1.20	79 %	PCL ₃₁ (-RhB)-CIPd(PET ₃) ₂
3	35	40	15.6	1.19	85 %	PPI ₃₀ (-RhB)-PCL ₃₀
4 ^d	35	40	16.7	1.21	87 %	PPI ₃₄ -PCL ₃₃
5 ^e	/	40	5.80	1.20	88 %	mPEG-PCL ₃₄

^aInitial feed ratio of monomers to catalyst. ^bM_n and M_w/M_n values were determined by SEC analyses with equivalent to polystyrene standard. ^cIsolated yields. ^dThis sample was prepared by a one-pot living polymerization of M₁ and M₂ with a reported Pd(II) complex (CIPd(PET₃)₂-OH). ^eThis sample was prepared by a ring-opening polymerization of M₂ using mPEG-OH (mPEG-OH; M_n = 1,900 g/mol) as a macroinitiator.

The proton signals attributed to RhB moieties, PPI blocks, and PCL blocks could be clearly distinguished in the ¹H NMR spectra (Figure 1B) of the copolymers. The block ratio of PPI and PCL was deduced to be approximately 1 to 1. After polymerization, in the ³¹P NMR spectrum, the peak of the catalyst at δ 17.8 ppm was replaced by a new doublet at 14.7 ppm, which corresponded to the formation of the polymers (Figure 1C).^[37] The FT-IR spectra of PM, CIPd(PET₃)₂(-RhB)-PCL, and PPI(-RhB)-OH samples showed a series of characteristic vibrations coming from both of PPI and PCL blocks (Figure S3). On the basis of such a detailed characterization, the expected amphiphilic PM

diblock copolymers were successfully obtained.

The morphology of PM copolymers in the solid state dried from THF solution was characterized by atomic force microscopy (AFM) in Figure 1D. Left- or right-handed helical nanofibrils with approximately 50-60 nm were clearly observed, resulting from the inherent properties of helical PPI chains. The copolymers were able to self-assemble (with a critical micelle concentration value of 8.65 mg/L measured by equilibrium surface tensions) by the gradual addition of pure water into dimethyl formamide (DMF) solution. The PM copolymers showed a size distribution ranging from approximately 9 to 13 nm in THF solution (Figure 1E), which was slightly larger

than those of PPI(-RhB)-OH and CIPd(PET₃)₂(-RhB)-PCL. However, the size of copolymers was ~77 nm in the aqueous dispersion. The morphology was further corroborated by transmission electron microscope (TEM) in Figure 1F, revealing the formation of spherical nanoparticles with diameters of ~60 nm. The size was in good agreement with dynamic light scattering (DLS) measurement.

Using THF as a co-solvent, PM copolymers, CPT drugs, and IR780 dyes could assemble into a single micelle. As shown in Figure 1G the ICM exhibited a strong absorbance at 355 nm for CPT, 558 nm for RhB, and 798 nm for IR 780, indicating the successful loading of NIR-absorbing dyes and anticancer drugs in the micelles. After the dosage of IR780, CPT, and PPI(-RhB)-PCL was adjusted, the micelles with a dye/drug/polymer ratio of 1/2/10 exhibited the highest encapsulation efficiency (IR780: ~80.32%; CPT: ~70.83%) and loading content (IR780: ~3.6%; CPT: ~6.3%). The emission spectrum of the ICM in water was also analyzed (Figure 1H), showing the maximum emission peak at ~828 nm. TEM observation (Figure 1I) showed a spherical micellar structure with a slightly larger size (~90 nm diameter) than that of PM (Figure 1F). To test the long-term stability, the size variation of the micelles in water

during 10 days was assessed using DLS (Figure S4). No significant size change or precipitation occurred during this period, indicating the excellent stability of ICM.

Sensitive pH-response and high cell-penetrating of helical diblock copolymers

To determine the cell membrane permeability of artificial synthetic helical PPI chains, mPEG-PCL and PPI-PCL were prepared. The ¹H NMR and SEC spectra are shown in Figure S5 and the detailed molecular parameters are summarized in Table 1. After model molecules (Nile red) were assembled, Nile red@mPEG-PCL (CM1) and Nile red@PPI-PCL (CM2) spherical micelles were obtained (Figure S6). After incubation of CM1 with HeLa cells, the intracellular fluorescence intensity showed obvious red emission at 100 min and tended to much brighter at 150 min. However, the CM1 treated cells displayed weaker fluorescence intensity even at 150 min (Figure 2A). As expected, CM2, which had a similar chemical structure, size distribution and helical chains to PM, revealed faster cell membrane permeability compared with CM1. It could be envisaged that a micelle shell with hydrophilic helical chains protruding out would also accelerate the penetration rate of cell membranes.

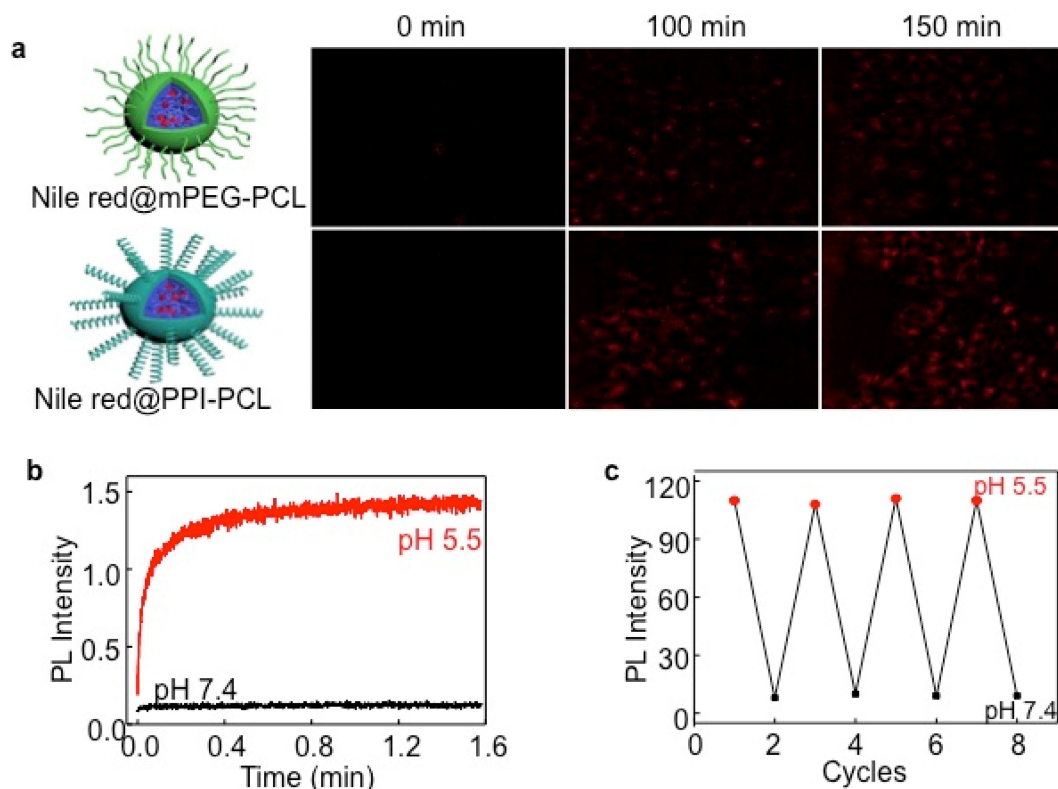


Figure 2. (A) Incubation duration-dependent CLSM images of live HeLa cells when culturing at 37 °C with Nile red@mPEG-PCL and Nile red@PPI-PCL micelles. The red channel was excited at 550 nm. (B) Typical time dependence of the emission intensity recorded during the ring-opening reaction of RhB moieties in PM induced by a stopped-flow pH jump from 7.4 to 5.5. (C) Change in the fluorescence emission intensity of PM at 25 °C when micellar dispersion pH was cycled between 5.5 and 7.4.

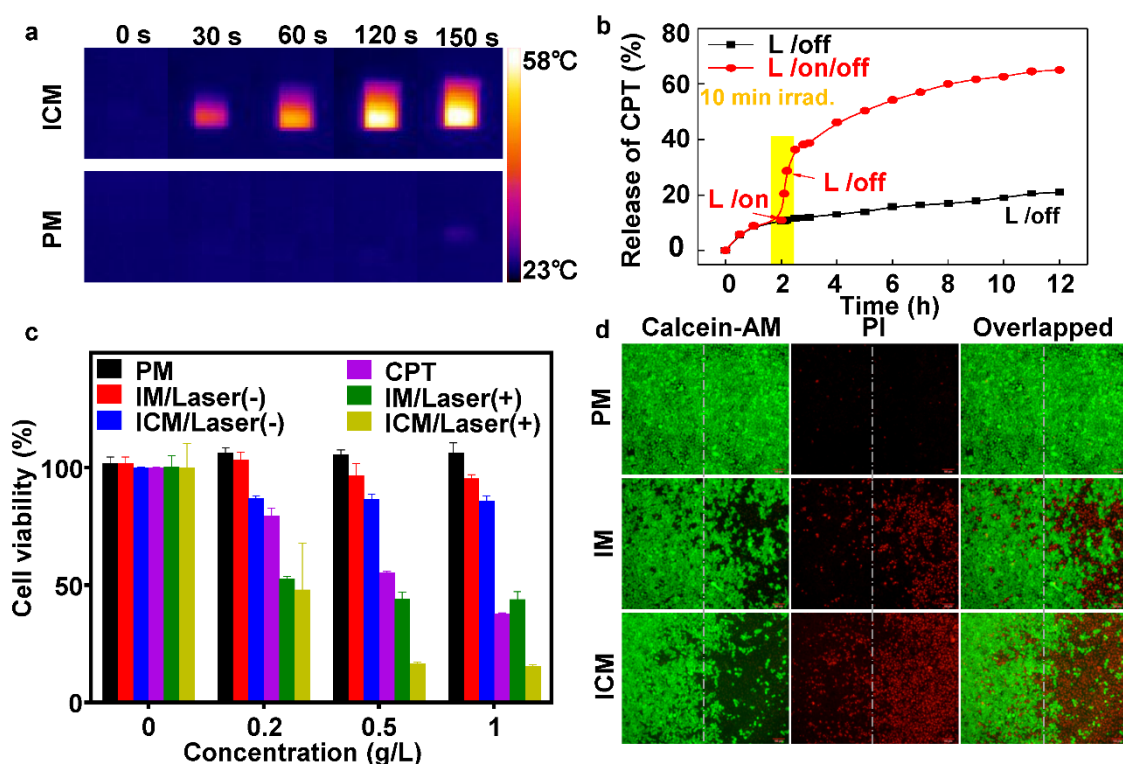


Figure 3. (A) NIR thermal imaging of ICM and PM after treated by 808 nm laser at power density of 1 W cm^{-2} for 150 seconds. (B) The CPT release profile of ICM with and without laser irradiation (808 nm, 1 W cm^{-2}) for 12 h. (C) The viability of HeLa cells treated with (+; for 10 min) or without (-) laser irradiation after being incubated with various micelles and concentrations. The error bars are based on the standard deviations of five parallel samples. (D) Fluorescence images of calcein AM/PI co-stained HeLa cells after incubation with PM, IM, and ICM upon being exposed to 808 nm laser at power density of 1 W cm^{-2} for 10 min (right side). Cells incubated with the same concentration (0.5 g/L) of polymeric micelles without laser irradiation were chosen as controls (left side).

In numerous studies, nonfluorescent RhB moieties were subjected to a selective ring-opening reaction when solution pH values were lowered, producing highly fluorescent RhB(H⁺) species. To clarify this reaction, a stopped-flow pH-jump technique was employed and the time-resolved fluorescence intensity change of PM was monitored. For a pH jump from 7.4 to 5.5, the fluorescence intensity exhibited an abrupt increase within the initial 0.2 min and kept stable within 1.6 min (Figure 2B). The fully reversible nature of pH-induced switching was verified by fluorescence measurements (Figure 2C). HeLa cells were then incubated with ICM with incubation time extended from 0 to 5 h. Figure S7 clearly showed an enhanced red fluorescence. By virtue of pH-responsive RhB moieties, ICM showed potential applicability for fluorescence bioimaging in the acidic tumor microenvironment.

In vitro photothermal efficiency and cytotoxicity

To evaluate the photothermal efficiency, ICM and PM were exposed to 1 W/cm^2 laser irradiation ($\lambda = 808 \text{ nm}$) for 150 seconds (Figure 3A). The temperature of PM increased by only $\sim 2^\circ\text{C}$, however, the temperature induced by the ICM increased to ~ 59

$^\circ\text{C}$, which could lead to fatal and irreversible damage to cancer cells (Figure S8A). After NIR laser irradiation, the stability of ICM was tested. Scanning electron microscope (SEM) observations (Figure S8B) revealed that the ICM were disrupted into flattened unordered aggregates instead of their initial spherical morphology. The result confirmed that the localized heating generated by the absorbing IR780 moieties was sufficient to affect the stability of the micelles. Then the hosted chemotherapeutic drugs could diffuse out from the micelle core and generate a potential synergistic effect with photothermal treatment.

The quantitative relationship between the released drugs and the laser irradiation time was then examined. In Figure 3B, without laser irradiation, the percent of CPT released from ICM was approximately 20% after 12 h, indicating minimal undesirable drug leaking. However, upon 10 min laser irradiation, ICM showed enhanced release of CPT up to 65% during the same period. The drug release rate grew twofold after laser irradiation, which mainly due to the destroyed micellar structure under photothermal effect. Meanwhile the drug releasing rate and dosage could be easily controlled by turning a laser on or off, allowing efficient remote laser-controlled drug release.

In the next step, the dose-dependent cytotoxicity of CPT, PM, IM, and ICM were systematically investigated by MTT assay. After incubating HeLa cells with different concentrations of micelles, Figure 3C clearly showed that those micelles had negligible cytotoxicity without NIR irradiation. Nevertheless, under laser irradiation, the IM micelles exhibited a remarkable photothermal effect compared without irradiation, especially at high micelle concentrations. The ICM enhanced the release of CPT drugs by laser irradiation, causing an extra boost in cell toxicity. Cell injury was further assessed by calcein-AM or propidium iodide (PI) staining. As shown in Figure 3D, 50% of the cells were killed by IM after 10 min of irradiation (808 nm, 1 W cm⁻²). Whereas most of the cells (~80%) were killed by ICM under the same conditions. This result indicated that the IR780 and CPT loaded micelles had not only excellent photothermal effects but also a synergistic chemotherapy effect.

In vivo multimodal imaging and biodistribution

Inspired by the low cytotoxicity (without NIR irradiation), excellent water dispersibility, NIR absorption properties of ICM, long circulation time in plasma (Figure S9), and imaging capability were further conducted *in vivo*. Fluorescence imaging on mice was used to study the distribution of ICM in

mice. At 8 h after intravenous injection, the ICM were distributed in the whole body and an obvious NIR fluorescent signal was detected at the tumor site (Figure 4A). Prolonging the observation time over 24 h, the fluorescence signals gradually accumulated in the tumor sites due to the EPR effect. However, 36 h after injection, the signal intensity decreased in the tumor tissue. This indicated that the ICM had begun to metabolize. In contrast, no NIR fluorescent signals could be detected in the PM injected group during the observation time. These results showed that the resultant ICM were efficient contrast agents for *in vivo* tumor NIR fluorescence imaging. The correlated NIR fluorescent intensities and contrast index (CI) values are shown in Figure 4B. After 24 h, the tumors and normal organs (heart, liver, spleen, lung, and kidney) were excised to evaluate the tissue distribution of ICM (Figure 4C) with signal intensities quantified in Figure 4D. The results revealed that the enriched NIR fluorescent signals of ICM accumulated primarily at tumor sites. The fluorescent signals in the liver and lung regions were also detected. These findings are attributable to the metabolism of ICM through the liver. The micelles signal in the lung can be explained by retention of a portion of ICM by capillaries in the lung.

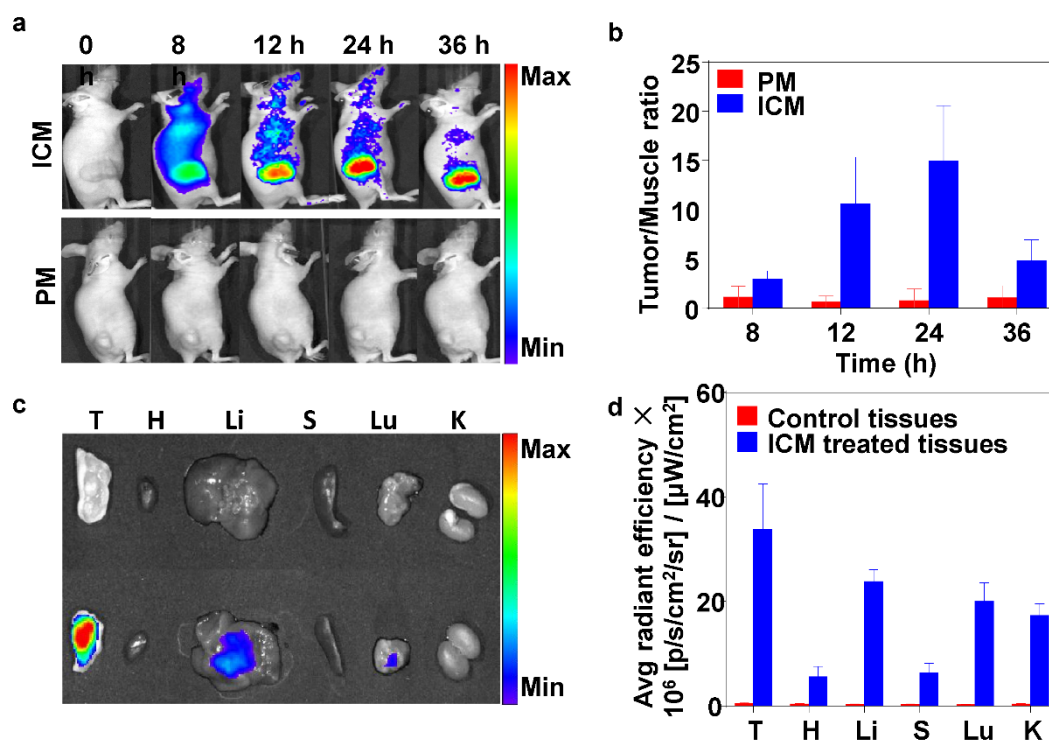


Figure 4. (A) Time-lapse NIR fluorescence (NIRF) images in mice taken at different times after intravenous injection of PM or ICM (200 μL, 2.0 g/L). (B) NIRF intensities and contrast index (CI) values quantified at the indicated time points (Tumor/Muscle ratio). (C) NIRF images taken for tumor and normal organs [tumor (T), heart (H), liver (Li), spleen (S), lung (Lu), kidney (K)] and (D) the quantification of CI values 24 h after the intravenous injection of PM or ICM.

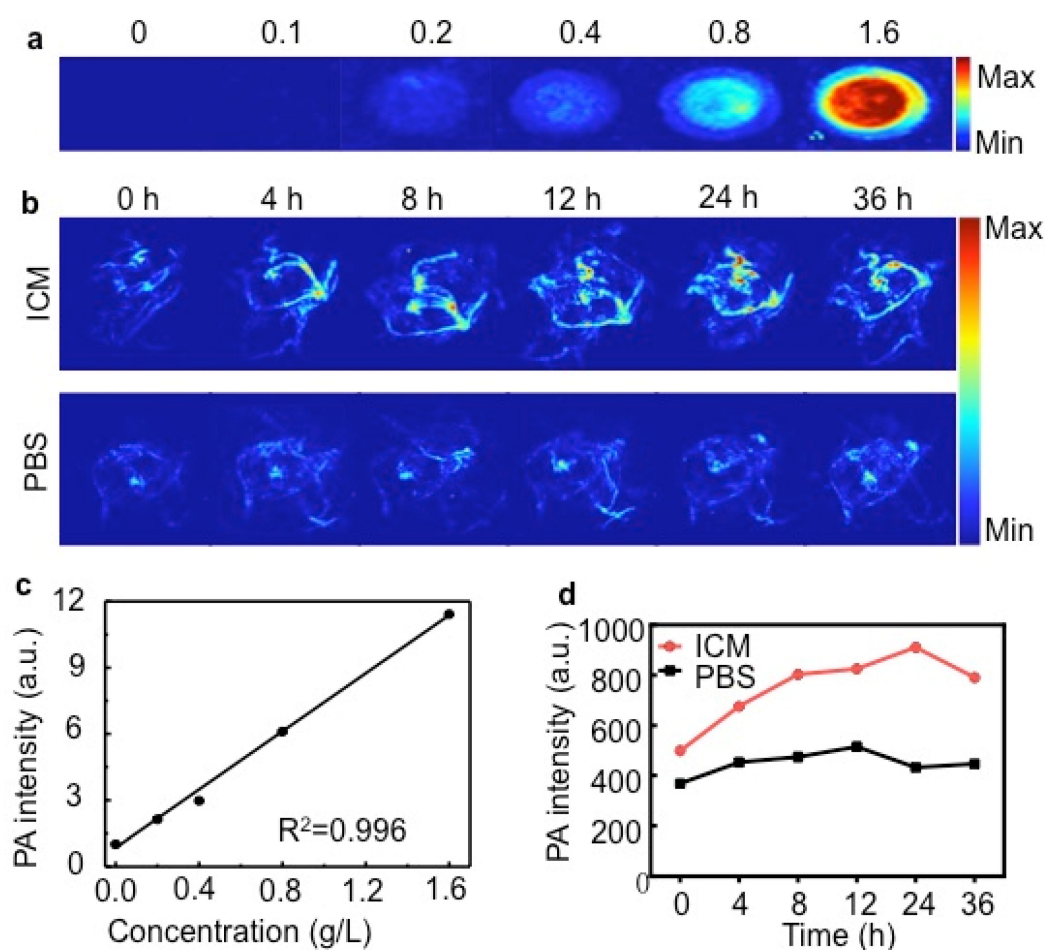


Figure 5. (A) PA images of ICM at different concentrations (g/L). (B) PA MAP images obtained for mice after intravenous injections of IR-780 micelles or PBS (C) PA intensity as a function of ICM at different concentrations. (D) Corresponding PA intensity of ICM and PBS buffer in tumor sites at different time points.

Here, the *in vitro* PA effect of ICM was shown in Figure 5A. The PA signals of ICM were evaluated as a function of concentrations and the signal exhibited a prominent linear increase with a $R^2 = 0.996$ (Figure 5C). Such a significant PA contrast effect prompted us to use ICM to visualize the tumor morphology and microvascular distribution *in vivo*. As shown in Figure 5B and Figure 5D, the PA signals in the tumor sites increased with time, and the highest intensity was detected 24 h after injection. Then normal organs were isolated to evaluate the tissue distribution of ICM (Figure S10). The liver and lung regions exhibited obvious signal enhancement compared with control groups, which was in accordance with the results of NIR fluorescence imaging (Figure 4C).

Chemo-photothermal synergistic therapy and tumor ablation

Although chemotherapeutic agent can achieve good antitumor effects, multiple and high doses are always required and are inevitably accompanied by side effects. The encapsulation of drugs in the micelle cores can remarkably decrease these side effects, but it

does not have a long-term therapeutic effect resulting from the insufficient drug release in tumor sites. To overcome the limitation of conventional chemotherapy, the synergistic efficacy of PTT and chemotherapy was realized in mice by injection of ICM. 24 h after injection, HeLa tumor-bearing mice were exposed to irradiation with an 808 nm laser (1 W/cm²) for 5 min (Figure 6A). The tumor temperature of the ICM treated group was higher than that of the PM group, maintaining a maximum temperature of 52.6 °C (Figure 6B). The temperature exceeded the damage threshold and induced irreversible tumor damage, indicating the good photothermal performance of ICM *in vivo*. Detailed *in vivo* NIR thermal images for ICM or PM micelle-treated mice as a function of irradiation time were shown in Figure S11.

A single dose of ICM to laser irradiation not only caused tumor necrosis by PTT but also simultaneously enhanced the CPT release from the micelle cores due to the thermo-sensitive PCL cores. The synergistic therapy, in principle, could completely eliminate the tumors or inhibit the

regrowth rate to a large extent. Seven days after the laser irradiation, the mice still showed obvious injury at the irradiation site. After 14 days of treatment, almost all the tumors in the ICM micelle-treated mice had disappeared without recurrence observed (Figure 6C). By comparison, the tumors in the IM micelle-treated mice suffered from mild regrowth around the black scar after 10 days, probably due to the insufficient therapy efficacy. Moreover, under the same irradiation, the tumors of the PM micelle-treated group showed negligible therapeutic efficiency and exhibited a growth rate as PBS control group. Figure 6D illustrated that no recurrence occurred in the ICM micelle-treated group as compared with the other three groups.

We also evaluated the potential toxic side effect of these micelles. No obvious body weight loss was observed in any of the groups, suggesting that a single-dose treatment did not cause significant adverse effects (Figure S12). The treated organs were then excised for hematoxylin and eosin (H&E) staining. In the normal organs, the histological section showed no obvious lesions. In contrast, tumor cells of ICM group and IM group had lost their complete morphology under NIR laser irradiation (Figure S13). These results once again verified that the ICM had excellent theranostic capabilities in a single-dose treatment and did not cause noticeable toxic side effects *in vivo*.

Conclusion

In conclusion, we have successfully developed an *in vivo* multi-modal imaging-guided chemo-photothermal integrated platform based on ICM polymers. The helical structure on the micelle surface endowed them with superior cell membrane permeability, which could promote them to simultaneously deliver CPT and IR780 to tumor regions. As an effective helical polymer, PPI shares structural and functional similarity to CPPs. However, hydrophilic helical PPI micelles are electrically neutral and have prolonged circulation time *in vivo*. Compared with positively charged CPP, electrically neutral PPI prevents PM from non-specific absorption of protein during circulation. The fluorescent and PA signals could be monitored to evaluate biodistribution of the micelles and reconstruct the morphology of the tumor sites. The synergistic effect of photothermal therapy and remote laser-controlled chemotherapy led to complete ablation of tumors without recurrence observed. By virtue of the inherent biocompatibility of PEGylated PI materials and the aforementioned multi-functions, the current formulation of our smart micelles with distinct hydrophilic helical chains on the surface may be promising for future clinical applications.

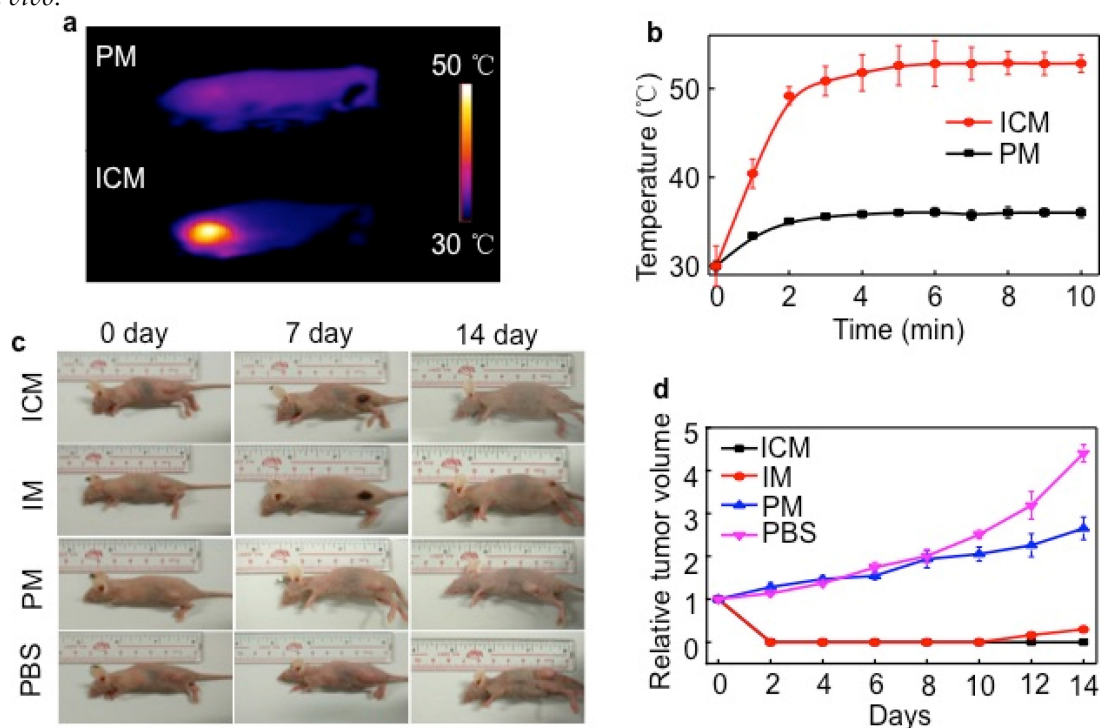


Figure 6. (A) *In vivo* NIR thermal imaging obtained 24 h after the intravenous injection of PM or ICM (200 μ L, 2.0 g/L) into mice and treatment by an 808 nm laser at a power density of 1 W cm^{-2} for 10 min. (B) Temperature change at the tumor sites as a function of irradiation time. (C) Effects of photothermal therapy in HeLa tumor-bearing mice. Representative time-dependent photos taken for mice after being irradiated by 808 nm NIR light with ICM, IM, PM (200 μ L, 2.0 g/L), and PBS post-injection. (D) Tumor volumes of different groups measured after laser irradiation and normalized to their initial size ($n = 5$ per group). Error bars indicated the means and standard errors.

Abbreviations

CLSM: Confocal laser scanning microscopy; CM: CPT@PPI(-RHB)-PCL; CPPs: Cell-penetrating peptides; CPT: Camptothecin; DLS: Dynamic light scattering; DMF: Dimethyl formamide; EB: Evans blue; EPR: Enhanced permeability and retention; ICG: Indocyanine green; ICM: IR780/CPT@PPI(-RHB)-PCL; IM: IR780@PPI(-RHB)-PCL; MB: Methylene blue; MTT: 3-(4,5-dimethyl-2-thiazolyl)-2,5-diphenyl tetrazolium bromide; MWs: Molecular weights; NIR: Near infrared; PAI: Photoacoustic imaging; PEG: Polyethylene glycol; PI: Phenyl isocyanide; PM: PPI(-RHB)-PCL; PPI: Phenyl isocyanide; PTT: Photothermal therapy.

Supplementary Material

Scheme S1 and Figures S1-S13.

<http://www.thno.org/v06p2170s1.pdf>

Acknowledgements

This work was supported by National Natural Scientific Foundation of China (51303044, 81571744, and 81301257), the National Basic Research Program of China (863 Program 2015AA020502), the Natural Scientific Foundation of Anhui Province (1408085QE80), Science Foundation of Fujian Province (No. 2014Y2004), and Xiamen University Startup (0260-ZK1029). J.Y. expresses his thanks for Specialized Research Fund for the Doctoral Program of Higher Education (20130111120013).

Competing Interests

The authors have declared that no competing interest exists.

References

- Wang LV, Hu S. Photoacoustic tomography: in vivo imaging from organelles to organs. *Science*. 2012; 335: 1458-62.
- Nie L, Wang S, Wang X, Rong P, Ma Y, Liu G, et al. In vivo volumetric photoacoustic molecular angiography and therapeutic monitoring with targeted plasmonic nanostars. *Small*. 2014; 10: 1585-93, 441.
- Pu K, Shuhendler AJ, Jokerst JV, Mei J, Gambhir SS, Bao Z, et al. Semiconducting polymer nanoparticles as photoacoustic molecular imaging probes in living mice. *Nat Nanotechnol*. 2014; 9: 233-9.
- Hannah A, Luke G, Wilson K, Homan K, Emelianov S. Indocyanine green-loaded photoacoustic nanodroplets: dual contrast nanoconstructs for enhanced photoacoustic and ultrasound imaging. *ACS nano*. 2014; 8: 250-9.
- Liu Y, Nie L, Chen X. Photoacoustic molecular imaging: from multiscale biomedical applications towards early-stage theranostics. *Trends in Biotechnology*. 2016; 34(5): 420-433.
- Liu Y, Kang N, Lv J, Zhou Z, Zhao Q, Ma L, Chen Z, Ren L, and Nie L. Deep photoacoustic/optical/magnetic resonance multimodal imaging in living subjects using high-efficient upconversion nanocomposites. *Advanced Materials*. 2016; doi: 10.1002/adma.201506460.
- Zhang C, Wang S, Xiao J, Tan X, Zhu Y, Su Y, et al. Sentinel lymph node mapping by a near-infrared fluorescent heptamethine dye. *Biomaterials*. 2010; 31: 1911-7.
- Yue C, Liu P, Zheng M, Zhao P, Wang Y, Ma Y, et al. IR-780 dye loaded tumor targeting theranostic nanoparticles for NIR imaging and photothermal therapy. *Biomaterials*. 2013; 34: 6853-61.
- Lu C, Das S, Magut PK, Li M, El-Zahab B, Warner IM. Irradiation induced fluorescence enhancement in PEGylated cyanine-based NIR nano- and mesoscale GUMBOS. *Langmuir: the ACS journal of surfaces and colloids*. 2012; 28: 14415-23.

- Qiu X, Xu L, Zhang Y, Yuan A, Wang K, Zhao X, et al. Photothermal Ablation of In Situ Renal Tumor by PEG-IR780-C13 Micelles and Near-Infrared Irradiation. *Molecular pharmaceutics*. 2016; 13: 829-38.
- Fang YP, Chuang CH, Wu PC, Huang YB, Tzeng CC, Chen YL, et al. Amsacrine analog-loaded solid lipid nanoparticle to resolve insolubility for injection delivery: characterization and pharmacokinetics. *Drug design, development and therapy*. 2016; 10: 1019-28.
- Peng CL, Shih YH, Lee PC, Hsieh TM, Luo TY, Shieh MJ. Multimodal image-guided photothermal therapy mediated by 188Re-labeled micelles containing a cyanine-type photosensitizer. *ACS nano*. 2011; 5: 5594-607.
- Wilk KA, Zielinska K, Pietkiewicz J, Skolucka N, Choromanska A, Rossowska J, et al. Photo-oxidative action in MCF-7 cancer cells induced by hydrophobic cyanines loaded in biodegradable microemulsion-templated nanocapsules. *International journal of oncology*. 2012; 41: 105-16.
- Robinson JT, Tabakman SM, Liang Y, Wang H, Casalongue HS, Vinh D, et al. Ultrasmall reduced graphene oxide with high near-infrared absorbance for photothermal therapy. *Journal of the American Chemical Society*. 2011; 133: 6825-31.
- Deng H, Dai F, Ma G, Zhang X. Theranostic Gold Nanomicelles made from Biocompatible Comb-like Polymers for Radiochemotherapy and Multifunctional Imaging with Rapid Clearance. *Advanced materials*. 2015; 27: 3645-53.
- Chen Q, Wang X, Wang C, Feng L, Li Y, Liu Z. Drug-Induced Self-Assembly of Modified Albumins as Nano-theranostics for Tumor-Targeted Combination Therapy. *ACS nano*. 2015; 9: 5223-33.
- Qiu H, Gao Y, Du VA, Harniman R, Winnik MA, Manners I. Branched micelles by living crystallization-driven block copolymer self-assembly under kinetic control. *Journal of the American Chemical Society*. 2015; 137: 2375-85.
- Wang T, Wang D, Yu H, Wang M, Liu J, Feng B, et al. Intracellularly Acid-Switchable Multifunctional Micelles for Combinational Photo/Chemotherapy of the Drug-Resistant Tumor. *ACS nano*. 2016; 10: 3496-508.
- Yuan A, Qiu X, Tang X, Liu W, Wu J, Hu Y. Self-assembled PEG-IR-780-C13 micelle as a targeting, safe and highly-effective photothermal agent for in vivo imaging and cancer therapy. *Biomaterials*. 2015; 51: 184-93.
- Smith BA, Daniels DS, Coplin AE, Jordan GE, McGregor LM, Schepartz A. Minimally cationic cell-permeable miniature proteins via alpha-helical arginine display. *Journal of the American Chemical Society*. 2008; 130: 2948-9.
- Zhang Q, Tang J, Fu L, Ran R, Liu Y, Yuan M, et al. A pH-responsive alpha-helical cell penetrating peptide-mediated liposomal delivery system. *Biomaterials*. 2013; 34: 7980-93.
- Daniels DS, Schepartz A. Intrinsically cell-permeable miniature proteins based on a minimal cationic PPII motif. *Journal of the American Chemical Society*. 2007; 129: 14578-9.
- Tang H, Yin L, Kim KH, Cheng J. Helical Poly(arginine) Mimics with Superior Cell-Penetrating and Molecular Transporting Properties. *Chemical science (Royal Society of Chemistry: 2010)*. 2013; 4: 3839-44.
- Watson JD, Crick FH. Molecular structure of nucleic acids; a structure for deoxyribose nucleic acid. *Nature*. 1953; 171: 737-8.
- Appella DH, Christianson LA, Klein DA, Powell DR, Huang X, Barchi JJ, Jr., et al. Residue-based control of helix shape in beta-peptide oligomers. *Nature*. 1997; 387: 381-4.
- Cordovilla C, Coco S, Espinet P, Donnio B. Liquid-crystalline self-organization of isocyanide-containing dendrimers induced by coordination to gold(I) fragments. *Journal of the American Chemical Society*. 2010; 132: 1424-31.
- Dama M, Berger S. Polyisocyanides as a new alignment medium to measure residual dipolar couplings for small organic molecules. *Organic letters*. 2012; 14: 241-3.
- Kajitani T, Onouchi H, Sakurai S, Nagai K, Okoshi K, Onitsuka K, et al. Lattice-like smectic liquid crystal phase in a rigid-rod helical polyisocyanide with mesogenic pendants. *Journal of the American Chemical Society*. 2011; 133: 9156-9.
- Miyabe T, Iida H, Ohnishi A, Yashima E. Enantioseparation on poly(phenyl isocyanide)s with macromolecular helicity memory as chiral stationary phases for HPLC. *Chemical Science*. 2012; 3: 863-7.
- Wu ZQ, Qi CG, Liu N, Wang Y, Yin J, Zhu YY, et al. One-pot synthesis of conjugated poly(3-hexylthiophene)-b-poly(phenyl isocyanide) hybrid rod-rod block copolymers and its self-assembling properties. *Journal of Polymer Science A Polymer Chemistry*. 2013; 51: 2939-47.
- Shi SY, He YG, Chen WW, Liu N, Zhu YY, Ding YS, et al. Polypeptide-b-Poly(Phenyl Isocyanide) Hybrid Rod-Rod Copolymers: One-Pot Synthesis, Self-Assembly, and Cell Imaging. *Macromolecular rapid communications*. 2015; 36: 1511-20.
- Hasegawa T, Kondoh S, Kazunori Matsuura A, Kobayashi K. Rigid Helical Poly(glycosyl phenyl isocyanide)s: Synthesis, Conformational Analysis, and Recognition by Lectins. *Macromolecules*. 1999; 32: 6595-603.
- Xue YX, Zhu YY, Gao LM, He XY, Liu N, Zhang WY, et al. Air-stable (phenylbuta-1,3-dienyl)palladium(II) complexes: highly active initiators for living polymerization of isocyanides. *Journal of the American Chemical Society*. 2014; 136: 4706-13.
- Shiraishi Y, Miyamoto R, Zhang X, Hirai T. Rhodamine-based fluorescent thermometer exhibiting selective emission enhancement at a specific temperature range. *Organic letters*. 2007; 9: 3921-4.
- Hamid MH, Allen CL, Lamb GW, Maxwell AC, Maytum HC, Watson AJ, et al. Ruthenium-catalyzed N-alkylation of amines and sulfonamides using

- borrowing hydrogen methodology. *Journal of the American Chemical Society*. 2009; 131: 1766-74.
36. Shiraishi Y, Miyamoto R, Zhang X, Hirai T. Rhodamine-based fluorescent thermometer exhibiting selective emission enhancement at a specific temperature range. *Org Lett*. 2007; 9: 3921-4.
37. Xue Y-X, Zhu Y-Y, Gao L-M, He X-Y, Liu N, Zhang W-Y, et al. Air-Stable (Phenylbuta-1, 3-diynyl) palladium (II) Complexes: Highly Active Initiators for Living Polymerization of Isocyanides. *J Am Chem Soc*. 2014; 136: 4706-13.